ESAIM: Proceedings, Vol. 1, 1996, pp. 77–94
http://www.emath.fr/proc/Vol.1/

Transport Element Method for Axisymmetric Variable-Density Flow and its Application to the Spread and Dispersion of a Dense Cloud

Xiaoming J. Zhang
BlazeTech Corporation
21 Erie Street
Cambridge, MA, USA

Ahmed F. Ghoniem
Dept. of Mechanical Engineering
Massachusetts Institute of Technology
Cambridge, MA 02139, USA

Abstract

The Lagrangian transport element method for the solution of axisymmetric constant-density flow is extended to variable-density flow. In this method, thin vortex ring-elements of the Rankine type are used to discretize the vorticity field as well as the density gradient field. At the axis, since the ring element concept does not apply, several Hill's spherical vortices are used. A simple algebraic expression for determining the density gradient is derived. Using this expression, the rate of baroclinic vorticity generation in the vorticity equation can be easily obtained. The transport element method, free of using Boussinesq approximation and turbulent closure modeling, is used to simulate variable-density flows such as the spread and dispersion of an axisymmetric dense gas cloud following its sudden release. The results show that multiple large scale concentric rings are generated at the cloud surface. Most of the cloud material is associated with the spreading front where the largest and strongest ring is located. The generation of these rings is explained using the baroclinic-vorticity generation mechanism. The entrainment of surrounding air into the dense cloud is shown to occur mainly at the cloud top through the large-scale engulfment by the vortex rings. The results on the cloud dispersion pattern and the rate of the horizontal spreading of the cloud compare well with experimental observations.

1 Introduction

Public concern over the risk posed by the accidental release of hazardous materials has grown over the past decade [1, 13, 15]. The sudden release of hazardous industrial material usually produces a cloud which is denser than air. The information on the dispersion of these dense gases that is interest to a hazard analyst is mainly the distribution of concentration as a function of location and time. The case of the collapse and spread of an isothermal dense cloud over a smooth surface in calm air is of special interest. The initial state is a quiescent upstanding cylindrical cloud with volume V_o, radius R_o and height H_o. Its density ρ_o is uniform and greater than the air density ρ_a. The cloud temperature is the same as the ambient temperature.

Large scale field experiments, like the Thorney Island experiment (1982–83) [13], and laboratory experiments have been performed to study the dispersion of a dense cloud cylinder [8]. Figure 1 shows the Thorney Island experiment, where (a) is taken at the moment immediately before the dense cloud collapse; and (b) is a top view of the cloud shortly after its collapse. Figure 2 shows a laboratory experiment, in which 135 liters of Freon-12/air mixtures was released, at different view angles and times. It is frequently observed that, after a sudden release of heavy gas on the ground, its dispersion can be approximately divided into two stages. The first stage, during the collapse of the cloud and the formation of a toroidal vortex at the spreading front, is the acceleration and fast spreading stage. During this stage, most of the cloud material is contained within the vortex ring (see Figs. 1b and 2a, b). Sometimes, multiple concentric rings or waves, which continue to expand nearly axisymmetrically, are observed (see Fig. 2c). The dominant driving force for this first stage is the negative buoyancy of the dense cloud. In the second stage, the cloud acts more like a passive tracer and its dispersion is controlled by the ambient wind and atmospheric turbulence.

Since the major difficulty rests on the study of the first stage, on which the dispersion of the later stage depends, several analytical and numerical models have been developed. Detailed reviews can be found in [1] and [15]. Most often, these models contain too many free constants, such as the entrainment rates and the effective time delay, which are not easy to determine. The calculation of the maximum concentration still involves large uncertainty. Furthermore, most analytical models use the Boussinesq approximation, which may not be valid in practice since most gases of interest in the accidents are much heavier than air. Numerical models provide more detailed and accurate predictions of the cloud dynamics (England et al. [4], Chan et al. [2], Havens et al. [7], Jacobson et al. [9], Ermak et al. [5]). However, large numerical diffusion and the limited validity of the turbulence-closure formulation [3] for buoyant flows restrict the application of these models. Although the formation of the frontal vortex ring is recognized to be important, its description is still unsatisfactory [16].

In this work, we first extend the transport element method from constant-density flow to variable-density flow in the axisymmetric case. Then, the method is applied to simulate the dispersion of an axisymmetric dense cloud during the first stage. Performed without invoking turbulence models, the numerical calculation is intended to improve our understanding of the entrainment process, the effect of large density ratio between the dense gas and air, and the effect of the cloud aspect ratio between the diameter and the height of the initially cylindrical dense cloud.

2 Physical model and mechanism of vortex ring formation

In our numerical simulation, only the first stage of the dense cloud dispersion is considered and the following approximations are applied: (1) the buoyancy of the dense cloud dominates the flow dynamics, and atmospheric turbulence is negligible[1]; (2) the dense cloud is released on a flat terrain and the motion is axisymmetric; (3) the ground friction and heat transfer are negligible; (4) the thermodynamic effects, including heat capacity, air moisture, and condensation, are neglected; (5) the density of any fluid particle does not change with time, even though there is a spatial variation of density (variable-density). Based on these assumptions, the governing equations describing the collapse and dispersion of a dense cloud are:

$$\frac{1}{r}\frac{\partial}{\partial r}(ru)+\frac{\partial w}{\partial z}=0 \tag{1}$$

$$\frac{\partial u}{\partial t}+u\frac{\partial u}{\partial r}+w\frac{\partial u}{\partial z}=-\frac{1}{\rho}\frac{\partial p}{\partial r} \tag{2}$$

$$\frac{\partial w}{\partial t}+u\frac{\partial w}{\partial r}+w\frac{\partial w}{\partial z}=-\frac{1}{\rho}\frac{\partial p}{\partial z}-\frac{\rho_p g}{\rho} \tag{3}$$

---

[1] A criterion for this approximation may be expressed in terms of the Richardson number, the ratio of the gravitational slumping flow to atmospheric turbulence, $Ri=\frac{(\rho-\rho_a)g}{\rho_a}\frac{V^{1/3}}{u^{*2}}$, where ρ, V, u^* are the cloud density, cloud volume and the friction velocity of the ambient flow, respectively.

$$\frac{\partial\rho}{\partial t}+u\frac{\partial\rho}{\partial r}+w\frac{\partial\rho}{\partial z}=0 \tag{4}$$

where r and z are radial and vertical coordinates pointing outwards and upwards; u and w are the velocity components in these directions; t is the time measured from cloud release; p is the pressure; and $\rho_p=\rho-\rho_a$ is the density perturbation. For nondiffusive flow, a suitable boundary condition at the ground is

$$w=0 \text{ and } \frac{\partial\rho}{\partial z}=0, \quad \text{at } z=0. \tag{5}$$

The initial condition for the instantaneously released dense cloud is

$$u=w=0,$$

$$\rho=\begin{cases}\rho_o, & r\le R_o \text{ and } z\le H_o\\ \rho_a, & \text{anywhere else}\end{cases} \qquad \text{at } t=0. \tag{6}$$

We use the following dimensionless variables to normalize the above equations,

$$(r^*,z^*)=\left(r/V_o^{1/3},z/V_o^{1/3}\right) \tag{7}$$

$$(u^*,w^*)=\left(u/\sqrt{gV_o^{1/3}},w/\sqrt{gV_o^{1/3}}\right) \tag{8}$$

$$t^*=t\sqrt{\frac{g}{V_o^{1/3}}} \tag{9}$$

$$p^*=\frac{p}{\rho_a g V_o^{1/3}} \tag{10}$$

$$\rho_p^*=\frac{\rho_o-\rho_a}{\rho_a}=\frac{\rho_p}{\rho_a} \tag{11}$$

where $V_o=\pi H_o R_o^2$ is the initial volume of the dense cloud. The normalized governing equations (after omitting *) become

$$\frac{1}{r}\frac{\partial}{\partial r}(ru)+\frac{\partial w}{\partial z}=0 \tag{12}$$

$$\frac{\partial u}{\partial t}+u\frac{\partial u}{\partial r}+w\frac{\partial u}{\partial z}=-\frac{1}{1+\rho_p}\frac{\partial p}{\partial r} \tag{13}$$

$$\frac{\partial w}{\partial t}+u\frac{\partial w}{\partial r}+w\frac{\partial w}{\partial z}=-\frac{1}{1+\rho_p}\frac{\partial p}{\partial z}-\frac{\rho_p}{1+\rho_p} \tag{14}$$

$$\frac{\partial\rho_p}{\partial t}+u\frac{\partial\rho_p}{\partial r}+w\frac{\partial\rho_p}{\partial z}=0. \tag{15}$$

Defining a dimensionless vorticity, taken positive in the anticlockwise direction if viewing downwards, $\omega = \frac{\partial u}{\partial z} - \frac{\partial w}{\partial r}$, and cross differentiating the momentum equations (13) and (14), we get the vorticity transport equation

$$\frac{D\omega}{Dt} = \frac{u\omega}{r} - \frac{1}{(1+\rho_p)^2}\left(\frac{\partial \rho_p}{\partial r}\frac{\partial p}{\partial z} - \frac{\partial \rho_p}{\partial z}\frac{\partial p}{\partial r}\right) + \frac{1}{(1+\rho_p)^2}\frac{\partial \rho_p}{\partial r} \tag{16}$$

where $D/Dt = \partial/\partial t + u\partial/\partial x + w\partial/\partial z$ is the substantial derivative. In deriving (2.4), the Boussinesq approximation has not been applied. In conservative form, Eq. 16 is

$$\frac{D(\omega/r)}{Dt} = \frac{G}{r} \tag{17}$$

where G, on the right hand side of the equation, is the baroclinic vorticity generation term:

$$G = \frac{-1}{(1+\rho_p)^2}\left(\frac{\partial \rho_p}{\partial r}\frac{\partial p}{\partial z} - \frac{\partial \rho_p}{\partial z}\frac{\partial p}{\partial r}\right) + \frac{1}{(1+\rho_p)^2}\frac{\partial \rho_p}{\partial r} \tag{18}$$

The components of the pressure gradient in (18) are obtained from Eqs. 13 and 14 as

$$\frac{\partial p}{\partial r} = -(1+\rho_p)\frac{Du}{Dt} \tag{19}$$

$$\frac{\partial p}{\partial z} = -(1+\rho_p)\frac{Dw}{Dt} - \rho_p \tag{20}$$

These equations will be solved by the axisymmetric transport element method, which will be described in detail in the next section.

From the vorticity equation (17), we know that the vorticity component in the circumferential direction is generated due to the misalignment of the surfaces of constant pressure and constant density, i.e., the non-zero baroclinicity expressed by Eq. 18. The major contribution to G initially is from the horizontal density gradient. At the moment of release of the dense cloud, the horizontal density gradient is very large. The term G is significant over the entire side wall of the cylindrical cylinder. The vorticity field induces a motion which pulls the cloud downwards and outwards (see Fig. 3). As the cloud front spreads, the circulation associated with the front ring gradually increases and rings of smaller sizes are also generated behind it.

3 Numerical schemes

3.1 The axisymmetric vortex method

The application of the vortex method to the solution of axisymmetric flow is based on the discretization of the vorticity field into a number of thin vortex ring elements[2] of finite volume and the transport of these elements along their corresponding trajectories. The method has been developed and used in the calculation of bluff-body flow dynamics [6]. The vortex ring element is chosen to be of the Rankine type, that is, the vorticity inside the ring's cross section is uniform ω_i and outside is zero. We denote $G_i = \omega_i \delta A_i$ as the circulation around the ith ring whose center is

---

[2] The vortex ring is thin if the radius of its cross section is much smaller than the radius of the ring.

located at $\chi_i = (\rho_i, \zeta_i)$ in any meridianal plane, where δA_i is the cross sectional area of the element, $\delta A_i = \pi \delta_i^2$, and δ_i is the core radius (see Fig. 4 for notation). The discretization can be written as

$$\omega(\mathbf{x}, t) = \sum_{i=1}^{N} \frac{\Gamma_i}{\delta A_i} \left[1 - H\left(\frac{|\mathbf{x} - \chi_i|}{\delta_i} \right) \right] \tag{21}$$

where $H(.)$ is the Heaviside function, which is one if the argument is greater or equal to 1 and zero otherwise. Since the continuity equation for an incompressible flow ensures the volume conservation of ring element, $\delta A_i \rho_i =$ constant, we obtain the following circulation equation for each vortex ring element from Eq. 17,

$$\frac{d\Gamma_i}{dt} = \delta A_i G \tag{22}$$

where G is the vorticity source term. If $G \neq 0$, the circulation of each element changes due to the generation of the baroclinic vorticity. The change is calculated based on an accurate evaluation of G which will be described in the section for the transport element method. The vortical velocity components at point $\mathbf{x} = (\rho, z)$ induced by a single vortex ring element located at χ_i, when $|\mathbf{x} - \chi_i| \geq \delta_i$, is calculated from [12],

$$u_i(\mathbf{x}, t) = \frac{-\Gamma_i}{2\pi r} \frac{(z - \zeta_i)(s_{1i} + s_{2i})}{s_{1i} s_{2i}} \left\{ K(\lambda_i) - \frac{E(\lambda_i)}{2} \left[\frac{s_{2i}}{s_{1i}} + \frac{s_{1i}}{s_{2i}} \right] \right\} \tag{23}$$

$$w_i(\mathbf{x}, t) = \frac{\Gamma_i}{2\pi r} \left\{ \left[\frac{r - \rho_i}{s_{1i}} + \frac{r + \rho_i}{s_{2i}} \right] [K(\lambda_i) - E(\lambda_i)] + \frac{s_{2i} - s_{1i}}{2} E(\lambda_i) \left[\frac{r + \rho_i}{s_{2i}^2} - \frac{r - \rho_i}{s_{1i}^2} \right] \right\} \tag{24}$$

where

$$s_{2i/1i} = \sqrt{(z - \zeta_i)^2 + (r +/- \rho_i)^2} \tag{25}$$

$$\lambda_i = \frac{s_{2i} - s_{1i}}{s_{2i} + s_{1i}}, \quad 0 \leq \lambda \leq 1 \tag{26}$$

$$K(\lambda) = \int_0^1 \left[(1 - t^2)(1 - \lambda^2 t^2) \right]^{-1/2} dt \tag{27}$$

$$E(\lambda) = \int_0^1 (1 - t^2)^{-1/2} (1 - \lambda^2 t^2)^{1/2} dt \tag{28}$$

A thin vortex ring travels in an unbounded, incompressible, frictionless flow with a self-induced velocity given by [17]:

$$u_{si} = 0 \quad \text{and} \quad w_{si} = \frac{\Gamma_i}{4\pi \rho_i} \left(\ln \frac{8\rho_i}{\delta_i} - 0.558 \right). \tag{29}$$

The induced velocity within the core, $|\mathbf{x} - \chi_i| < \delta_i$, is approximated by linear interpolation between (u_{si}, w_{si}) at the center of the core and the velocity calculated using Eqs. 23–28 at its outer edge, at point $\mathbf{x} = \chi_i + \delta_i \mathbf{e}$, where $\mathbf{e}$ is the unit vector in the direction of $\mathbf{x} - \chi_i$. Thus, the vortical velocity induced by N thin vortex ring elements is obtained from

$$u_\omega(\mathbf{x},t) = \sum_{i=1}^{N} u_i(\mathbf{x},t) \quad \text{and} \quad w_\omega(\mathbf{x},t) = \sum_{i=1}^{N} w_i(\mathbf{x},t). \tag{30}$$

This algorithm only holds for thin vortex rings, $\delta_i/\rho_i \ll 1$. In the situation when the vortex ring is not thin, the element's circular cross section can not be maintained and expressions (23)–(29) do not approximate the velocity accurately. The treatment of "fat" vortex rings can be facilitated using Hill's spherical vortex which is discussed in the next subsection.

3.2 Hill's spherical vortex

The induced velocity of a fat vortex ring element that has a very small radius, $\rho = 0$, is approximated using Hill's spherical vortex. A detailed description of the vortex structure can be found in [12]. A Hill's vortex with radius a and self-induced velocity U has circulation $\Gamma = \frac{5\pi}{2} U a$. Its induced velocity components outside of the vortex are:

$$u = \frac{3}{2} U r z \frac{a^3}{(r^2 + z^2)^{5/2}} \tag{31}$$

$$w = \frac{U a^3}{(r^2 + z^2)^{3/2}} - \frac{3}{2} \frac{U a^3 r^2}{(r^2 + z^2)^{5/2}} \tag{32}$$

Norbury [14] pointed out that the classical thin vortex ring as described above and the Hill's spherical vortex are two asymptotes of a family of vortex rings based on a single parameter $\alpha = \delta_{\mathit{eff}}/\rho$, where δ_{eff} is the radius of the cross section as if it were circular and with the same area, and ρ is the major radius of the ring. When $\alpha \to \sqrt{2}$, the vortex ring approaches a Hill's spherical vortex, when $\alpha \to 0$ it approaches thin vortex ring with circular cross section. Norbury's computation indicates that for $\alpha \leq 0.2$ the shape of the cross section of the vortex ring is indistinguishable from that of a circular. Knio and Ghoniem [11], through numerical calculation, found that Eq. 29 worked well for $\delta_i/\rho_i \leq 0.2$. Therefore, vortex ring with $\delta_i/\rho_i \leq 0.2$ can be considered as thin, and the induced vortical velocity field can be computed using Eqs. 23–29.

To reduce the computational effort, the collective effect of all fat vortex rings, with $\delta_i/\rho_i > 0.2$, is approximately accounted for by a Hill's spherical vortex with radius $a = 5\delta$, where δ is the largest of δ_i. The circulation of the Hill's vortex is the algebraic sum of the circulation of all the rings inside its radius. Since δ is of the same order of magnitude as the spatial resolution of the discretization, and since the flow near the axis does not involve much vorticity, $\omega = 0$, $\partial\rho/\partial r = 0$ and $u = 0$ on the axis, this approximation is reasonable. The induced vertical velocity w of Hill's vortex at $r = 0$ by ring elements outside its boundary seems to be singular in Eqs. 23–28. However, this singularity is removable. After some calculation using the L'Hospital's rule, the induced vertical velocity is

$$w(r=0) = \sum \frac{\Gamma_i \rho_i^2}{2 s_o^3} \tag{33}$$

where the summation is over all elements with $\delta_i/\rho_i > 0.2$.

3.3 Transport element method

In the transport element method, instead of directly discretizing the density field, we discretize the density gradient field $\mathbf{g} = \nabla \rho_p$ into a finite number of Lagrangian transport elements,

$$\mathbf{g}(\mathbf{x}, t) = \sum_{i=1}^{N} \mathbf{g}_i \left[1 - H\left(\frac{|\mathbf{x} - \chi_i|}{\delta_i} \right) \right] \tag{34}$$

where $\mathbf{g}_i$ is the density gradient of the flow field at the location of the ith element, as shown in Fig. 5. We assign layers which coincide with the density contours in any meridianal plane with increment $\delta\rho_p$. When the fluid motion is incompressible and nondiffusive, the density of a fluid particle does not change as it moves. Thus, the density increment $\delta\rho_p$ across any two layers does not change with time. The time variation of the density gradient according to the definition is

$$\mathbf{g}_i(t) = (\nabla \rho_p)_i(t) = \frac{\delta \rho_p}{\big(\delta n(t)\big)_i} \mathbf{n}_i(t) \tag{35}$$

where $\mathbf{n}_i(t)$ is the unit vector normal to the density contour at the location at the ith element, $\big(\delta n(t)\big)_i$ is the normal distance between the two adjacent density layers. We discretize the field into elements each with cross sectional area δA_i initially in the meridianal plane. The element area is characterized by the length $\big(\delta l(t)\big)_i$ along the density contour and $\big(\delta n(t)\big)_i$ as defined above. This cross section is deformed due to the fluid motion. Since the density of a fluid particle does not change as the flow evolves, mass conservation gives

$$\big(\delta n(t)\big)_i \big(\delta l(t)\big)_i \rho_i(t) = \delta A_i(0) \rho_i(0) \tag{36}$$

where $\rho_i(t)$ and $\rho_i(0)$ are the radii of the ring element at time t and $t = 0$, respectively. Upon substitution of the above into Eq. 35, we get

$$\mathbf{g}_i(t) = \frac{\delta \rho_p \big(\delta l(t)\big)_i}{\delta A_i(0)} \frac{\rho_i(t)}{\rho_i(0)} \mathbf{n}_i(t) \tag{37}$$

Since the quantities on the right-hand side of equation (3.13) can be obtained easily in our Lagrangian calculation, this scheme is both accurate and efficient.

3.4 Boundary conditions

The condition of zero normal flow, $w = 0$, at ground, $z = 0$, is satisfied by superimposing a counter-rotating vortex ring image for each vortex ring element. The image of the vortex ring element at $\chi_i = (\rho_i, z_i)$ with circulation Γ_i is at $\chi_{ie} = (\rho_i, -z_i)$ with circulation $-\Gamma_i$. The satisfaction of the zero normal density gradient at the ground $z = 0$ is implemented in a similar way.

4 Numerical results

To achieve accurate numerical results, we used the following numerical parameters: spatial discretization, $h = 0.05$, time marching step, $\Delta t = 0.01$, number of layers used to describe the large density gradient between the cloud and air, $L = 4$.

We performed numerical computations for five cases, whose parameters are shown in Table I. Cases 1, 2 and 3 have the same density ratio but different aspect ratio, and case 1, 4 and 5 have the same aspect ratio but different density ratio. Figure 6 shows the dispersion pattern of a dense

Table I. Parameters used in numerical experiments

Case	D_o/H_o	ρ_o/ρ_a	$R_o=D_o/2$	H_o
1	1	1.5	$1/\sqrt{2\pi}$	$\sqrt{2/\pi}$
2	2	1.5	$\sqrt[3]{2}/\sqrt{2\pi}$	$\sqrt[3]{2}/\sqrt{2\pi}$
3	3	1.5	$\sqrt[3]{3}/\sqrt{2\pi}$	$2\sqrt[3]{3}/3\sqrt{2\pi}$
4	1	4	$1/\sqrt{2\pi}$	$\sqrt{2/\pi}$
5	1	3	$1/\sqrt{2\pi}$	$\sqrt{2/\pi}$

cloud with same initial volume and: (a) small aspect ratio and small density ratio, $D_o/H_o = 1$, $\rho_o/\rho_a = 1.5$; (b) large aspect ratio and small density ratio, $D_o/H_o = 3$, $\rho_o/\rho_a = 1.5$; and (c) small aspect ratio and large density ratio, $D_o/H_o = 1$, $\rho_o/\rho_a = 4$. The evolution of these three cases generally shows the similar overall pattern: As the cloud height decreases, the horizontal extent increases quickly, a large and intense vortex ring is generated at the frontal edge of the spreading cloud, and several smaller rings are generated behind the frontal ring. The decrease of cloud height and the increase of the frontal radius show the conversion of initial potential energy into kinetic energy. Comparing (a) with (b), it is seen that for the same cloud-to-air density ratio and same amount of cloud material released, the tall cloud, being of small radius initially, spreads faster. This is because the initial potential energy associated with case (a) is larger. Similarly, having the same aspect ratio and initial cloud volume as case (a), the cloud in case (c) which has a larger density ratio collapses and spreads faster. With smaller initial potential energy, case (b) retains considerable portion of the cloud material behind the evolving rings.

The mechanism for the generation of the large-scale frontal vortex ring and several smaller rings has been explained using the baroclinic vorticity generation mechanism in Section 2. These rings play a very important role in the dispersion of the cloud material. As shown in Fig. 6, the frontal ring, being at the location of the largest radius from the center and with the largest height vertically, contains most of the cloud material, in accordance with the observations of both field and laboratory experiments. The generation of smaller rings behind the front was also a prevailing phenomenon in the laboratory experiment of Spicer and Havens [18]. The entrainment of surrounding air into the cloud is observed to be mostly through engulfment at the top side of the cloud.

Figure 7 shows case 5 at time $t^* = 7.7$ in terms of: (a) an enlarged frame of the rollup and convolution of the cloud-air interface; and (b) the position of the computational elements and their instantaneous velocity vectors. It is seen that the cloud material concentration is not uniform inside the rings, and thus considerable fluctuations maybe encountered in the experimental measurements of the concentration. This is because the mixing originates from the buoyancy generated turbulence, in contrast to a diffusion type mixing. Figure 7b shows that most of the computational elements are within the complex flow region, the rings; and fewer elsewhere, confirming the adaptivity of the numerical method.

The generation of baroclinic vorticity can also be measured quantitatively in terms of circulation associated with these vortex rings. Figure 8 shows the total circulation integrated over a meridianal plane for all five cases. The cloud with large initial potential energy generates the largest circulation, pulling the cloud downwards and outwards. Large initial potential energy is associated with larger initial density difference between the cloud and air, or a large area of side wall of the initial cylinder, to which baroclinic vorticity is proportional. It is also seen that in all five cases, the rate of increase of circulation slows down eventually. This is because of a reason similar to the one described in a buoyant plume rising in the atmosphere: Vorticity with opposite sense also develops after certain time [19].

Figure 9 shows the dimensionless cloud radial extent, $x^* = (R^2 - R_o^2)/V_o^{2/3}$, versus time,

$$t' \equiv t\sqrt{\frac{\rho_o - \rho_a}{\rho_a}\frac{g}{V_o^{1/3}}} \tag{38}$$

conventionally used in the laboratory and field experiments. This relation is of primary interest in practice because a large portion of cloud material is within the frontal head. In the calculation of the area covered by the cloud, the frontal radius is defined by the computational ring element with the largest radius. The figure shows that three cases with the same density ratio but different aspect ratio almost overlap, while the three curves with same aspect ratio but different density ratio diverge considerably. It can also be seen that all these five curves asymptote to a linear relation after a rather short initial adjustment process, beyond $t^* = 3$. This linear relation, of almost the same slope for all five cases, is well observed. Thus, the initial collapse only produces a shift at the beginning of the linear behavior. At the later stages, the difference among the five cases becomes negligible compared to the large magnitude of the extended area. This suggests that the aspect ratio and the density ratio can be approximately grouped into the normalized variables x^* and t^*.

The cloud height is an important parameter in the dispersion pattern. Figure 10 shows the evolution of the cloud height, defined as the height of the top computational element, for all five cases. It is seen that the height initially decreases rapidly and then approaches an asymptotic value. For the three cases with different initial height but same density ratio, the asymptotic height is almost the same, apart from a small fluctuation due to the turbulent nature of the flow. The asymptotic heights of the other two cases are only slightly higher. This agrees well with experimental measurements and validates the assumption of several theoretical models developed in the past that the cloud height approaches a constant value after the fast collapse. It should also be pointed out that the highest thickness of the dense cloud after the initial collapse, as shown in the figure, is mostly associated with the frontal ring. Therefore, the slumping frontal vortex ring has a fairly long-lived coherent structure and its vertical size is described by this asymptotic height.

Figure 11 shows a comparison between numerical result, the laboratory measurements and a theory developed elsewhere [20] in terms of dimensionless cloud radial extent versus time. Since cases 1, 2 and 3 almost overlap, see Fig. 9, we draw only cases 1, 4 and 5. The numerical computations are terminated before $t' = 5$, considering that the assumption of neglecting friction near the ground becomes gradually invalid. The numerical result compares well with the experimental measurements within the small range of collapse and initial spread of the dense cloud. Since the simulation neglects the ground friction which would slow down the spreading, the radial extent of the simulated clouds increases faster than that of the physical experiments beyond $t' = 4$.

5 Conclusion

In this work, the transport element method has been extended to the simulation of axisymmetric variable-density flow. The dispersion and collapse of a dense cloud after its sudden release is then studied numerically. The numerical model simulates the early dispersion process including the formation and evolution of a frontal vortex ring and the rings behind it. The entrainment of air into the dense cloud occurs mainly on the top side through the engulfment of air by the vortex rings developed along the cloud surface. The physical phenomena, revealed by the numerical results, compared well with laboratory and field observations. The effects neglected in this work, such as, atmospheric turbulence, heat transfer, and ground terrain, will be investigated in future work.

Acknowledgment

This work has been jointly supported by the Mineral Management Services of the Department of the Interior, and the Building and Fire Research Laboratory of the National Institute of Standards and Technology. The computer support for this project is provided by the Illinois National Center for Supercomputer Applications.

References

[1] Britter, R.E., "Atmospheric Dispersion of Dense Gases," *Ann. Rev. Fluid Mech.*, **21**, pp. 317–344, 1989.

[2] Chan, S.T., Ermak, D.L. and Morris, L.K., "FEM3 Model Simulation of Selected Thorney Island Phase I Trials," *J. of Haz. Mat.*, **16**, pp. 267–292, 1987.

[3] Eidsvik, K.J., "A Model for Heavy Gas Dispersion in the Atmosphere," *Atmos. Environ.*, **14**, pp. 769–777, 1980.

[4] England, W.G., Teuscher, L.H., Hauser, L.E. and Freeman, B.E., "Atmospheric Dispersion of Liquefied Natural Gas Vapor Clouds Using SIGMET, a Three-Dimensional Time-Dependent Hydrodynamic Computer Model," *Proc. 1978 Heat Transfer and Fluid Mech. Inst.*, edited by C.T. Crowe and W.L. Grosshandler, Stanford Univ. Press., Stanford, CA, pp. 4–20, 1978.

[5] Ermak, D.L. and Chan, S.T., "Recent Development on the FEM3 and SLAB Atmospheric Dispersion Models," in *Stably Stratified Flow and Dense Gas Dispersion*, edited by J.S. Puttock, Oxford: Clarendon, pp. 264–284, 1988.

[6] Ghoniem, A.F. and Martins, L.-F., "Effect of Velocity Ratio on Bluffbody Dynamics; Steady and Transitional Regimes," AIAA-91-0580, 1991.

[7] Havens, J.A., Schreurs, P.J. and Spicer, T.O., "Analysis and Simulation of Thorney Island Trial 34," *J. of Haz. Mat.*, **16**, pp. 139–148, 1987.

[8] Havens, J.A. and Spicer, T.O., Development of an Atmospheric Dispersion Model for Heavier-than-air Gas Mixtures, Volume II: Laboratory Calm Air Heavy Gas Dispersion Experiments, No. CG-D-23-85, 1985.

[9] Jacobsen, O. and Magnussen, B.F., "3-D Numerical Simulation of Heavy Gas Dispersion," *J. of Haz. Mat.*, **16**, pp. 215–230, 1987.

[10] Johnson, D.R., "Thorney Island Trials: Systems Development and Operational Procedures," in *Heavy Gas Dispersion Trials at Thorney Island*, edited by J. McQuaid, Elsevier, pp. 35–64, 1985.

[11] Knio, O.M. and Ghoniem, A.F., "Numerical Study of a Three-Dimensional Vortex Method," *J. Comp. Phys.*, **86**, pp. 75–106, 1990.

[12] Lamb, H., Hydrodynamics, 6th Edition, Dover Publications, New York, 1945.

[13] McQuaid, J. ed., Heavy Gas Dispersion Trials at Thorney Island, Elsevier, xii+435p., 1985.

[14] Norbury, J., "A Family of Steady Vortex Rings," *J. Fluid Mech.*, **57**, pp. 417–431, 1973.

[15] Puttock, J.S., ed., Stably Stratified Flow and Dense Gas Dispersion, Clarendon Press, Oxford, xiv+430p., 1988.

[16] Rottman, J.W. and Hunt, J.C.R., "The Initial and Gravity-Spreading Phases of Heavy Gas Dispersion: Comparison of Models with Phase I Data," in *Heavy Gas Dispersion Trials at Thorney Island*, edited by J. McQuaid, Elsevier, pp. 261–279, 1985.

[17] Saffman, P.G., "The Velocity of Viscous Vortex Rings," *Studies in Appl. Math.*, **49**, pp. 371–380, 1970.

[18] Spicer, T.O. and Havens, J.A., "Modeling the Phase I Thorney Island Experiments," in *Heavy Gas Dispersion Trials at Thorney Island*, edited by J. McQuaid, Elsevier, pp. 237–260, 1985.

[19] Zhang, X. and Ghoniem, A.F., "A Computational Model for the Rise and Dispersion of Wind-Blown, Buoyancy Driven Plumes. Part I. Neutrally Stratified Case," *Atmos. Environ.*, **27**, pp. 2295–2311, 1993.

[20] Zhang, X., A Computational Analysis for the Rise, Dispersion and Deposition of Buoyant Plumes, Ph.D. Thesis, Massachusetts Institute of Technology, Mechanical Engineering, 1993.

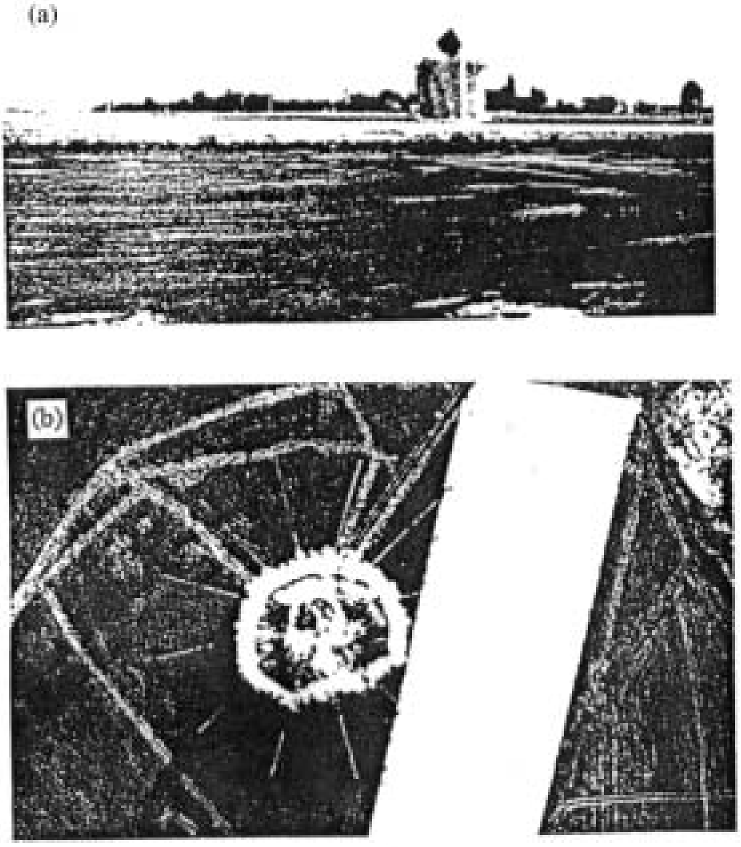

Figure 1: Thorney Island experiment: instantaneous dense gas release (a) viewed at ground level, (b) viewed from overhead, from Johnson [10].

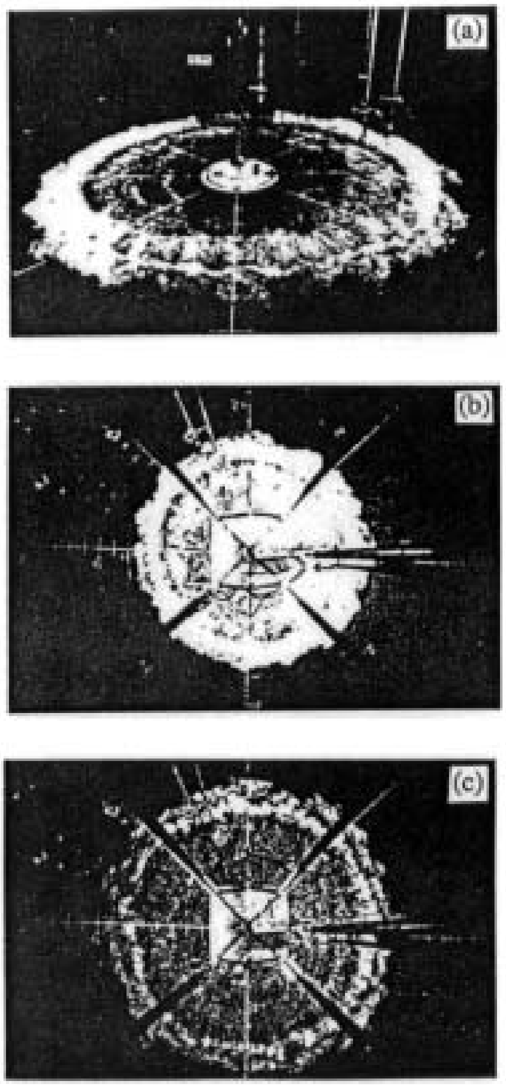

Figure 2: A case of laboratory experiment observed at different view angles and times after the instantaneous release of 135 liter Freon-12/air mixtures: (a) $t = 1.2$s; (b) $t = 1.2$s; (c) $t = 1.7$s, from Spicer and Haverns [18].

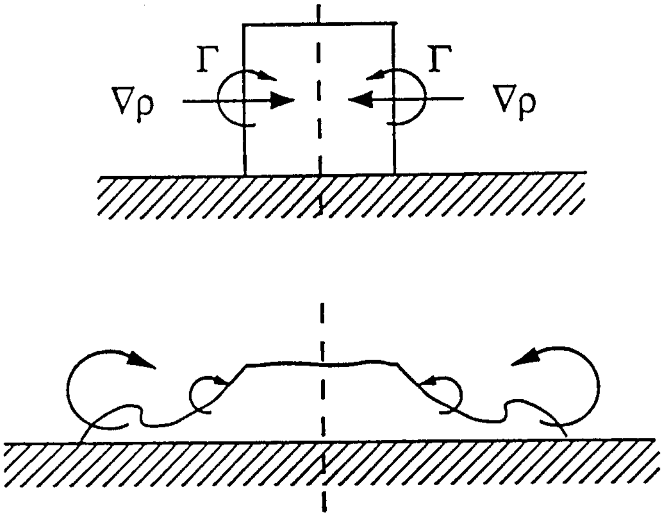

Figure 3: A schematic diagram showing the mechanism of baroclinic vorticity generation.

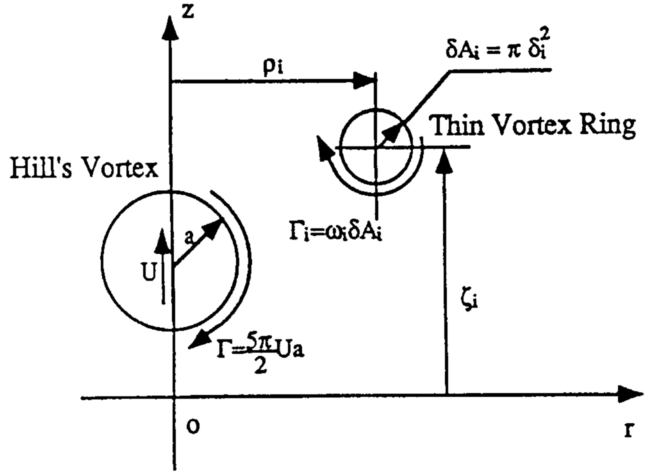

Figure 4: A schematic diagram describing the notations for the vortex ring element and Hill's spherical vortex.

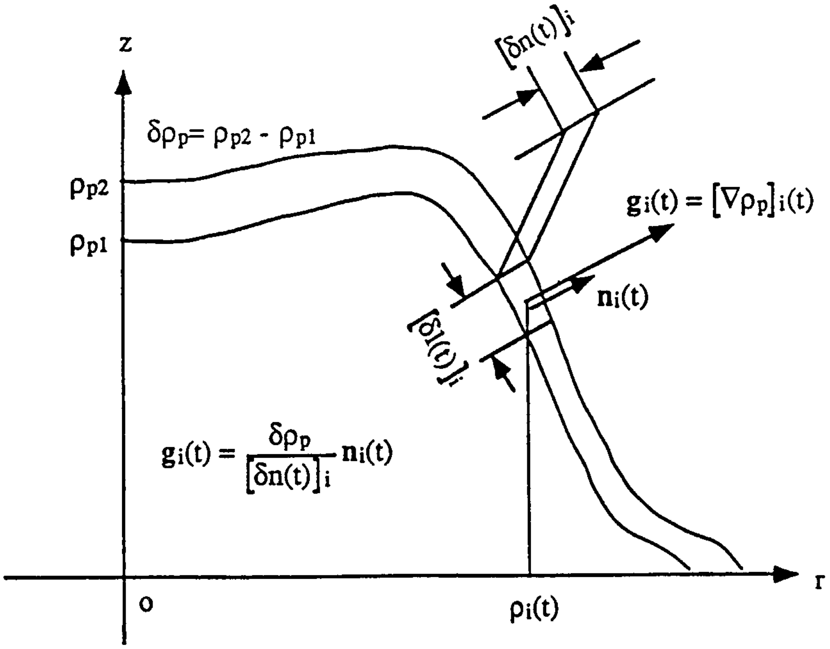

Figure 5: A schematic diagram showing the notations used for the derivation of transport element method in axisymmetric flow with variable density.

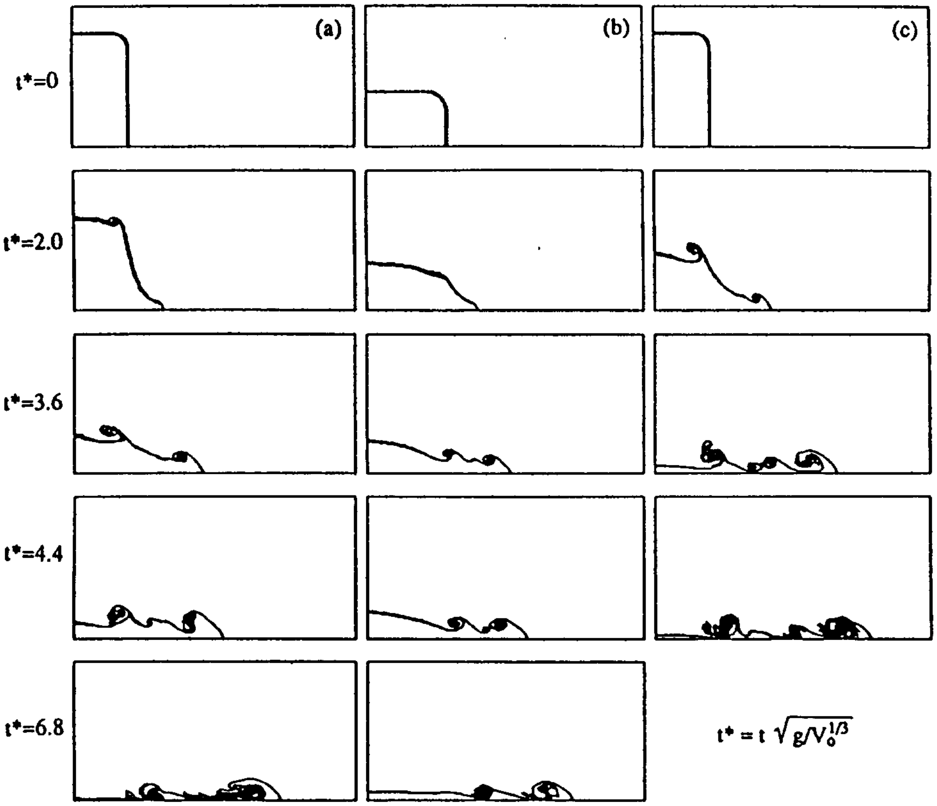

Figure 6: Results of three numerical simulations on the evolution of dense cloud collapse and spread in terms of cloud shape; (a) Case 1: $D_o/H_o = 1$, $\rho_o/\rho_a = 1.5$; (b) Case 3: $D_o/H_o = 3$, $\rho_o/\rho_a = 1.5$; (c) Case 4: $D_o/H_o = 1$, $\rho_o/\rho_a = 4$.

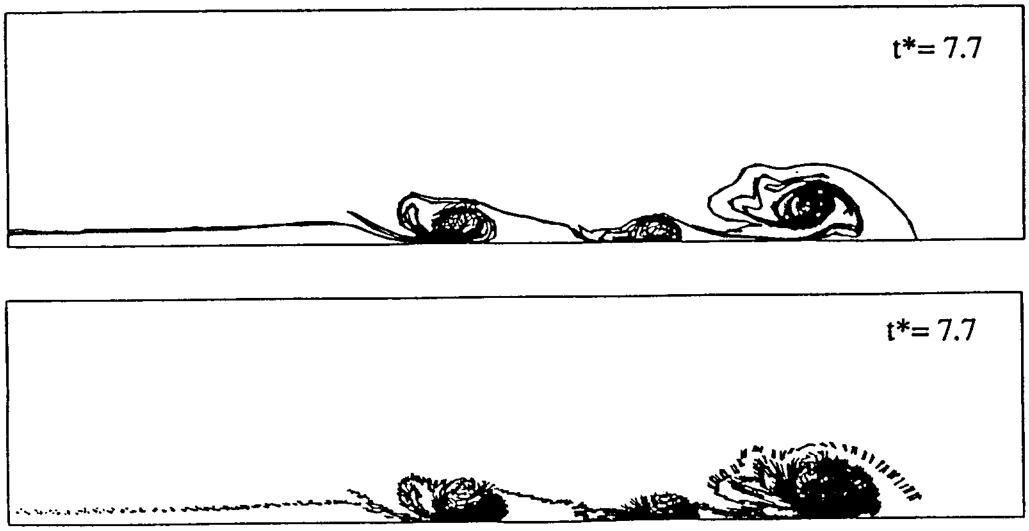

Figure 7: The cross sections of dense cloud spread for Case 5: $D_o/H_o = 1$, $\rho_o/\rho_a = 3$ at $t^* = 7.7$; (a) the cloud shape; (b) the positions and velocities of the computational elements.

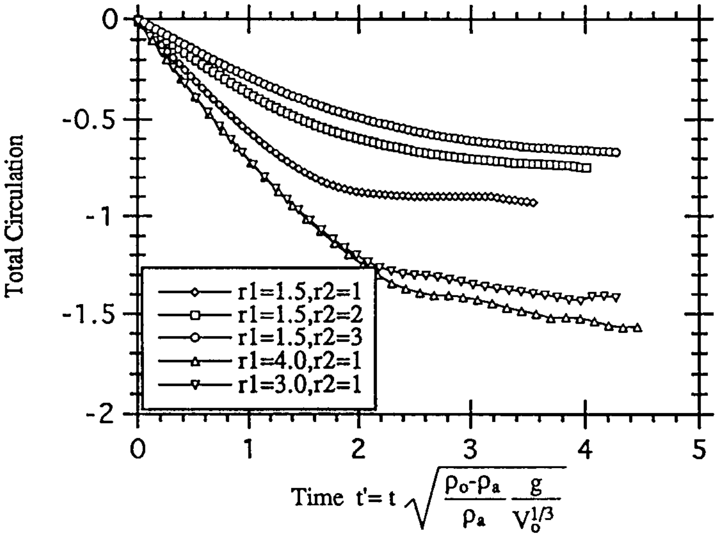

Figure 8: The evolution of the total circulation integrated over a meridional plane during the dense cloud collapse for the five cases, where $r1 = \rho_o/\rho_a$ and $r2 = D_o/H_o$.

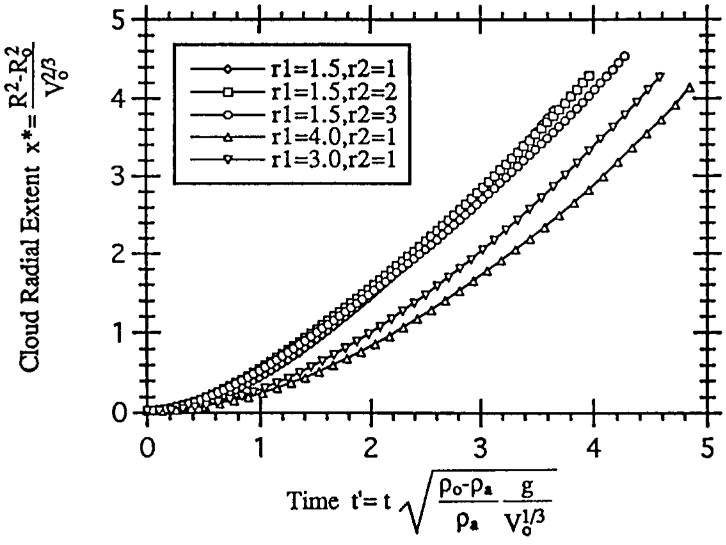

Figure 9: The increase in the top cloud area after the collapse of the dense cloud versus time, $t' \equiv \sqrt{\frac{\rho_o-\rho_a}{\rho_a}\frac{g}{V_o^{1/3}}}$, for five cases, where $r1 = \rho_o/\rho_a$ and $r2 = D_o/H_o$.

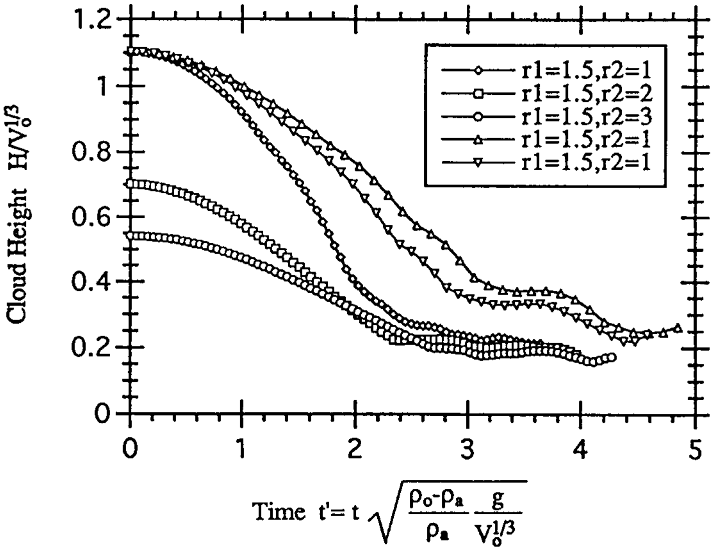

Figure 10: The maximum could height versus time for five cases, where $r1 = \rho_o/\rho_a$ and $r2 = D_o/H_o$.

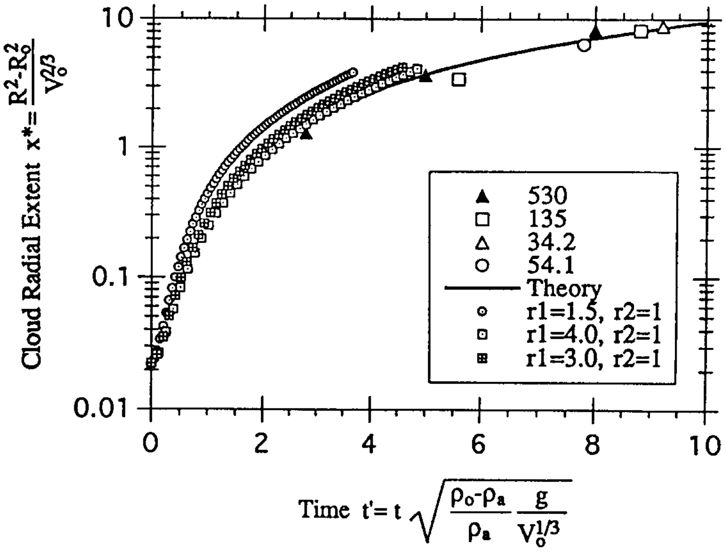

Figure 11: The increased top cloud area versus time. Comparison among numerical results, theoretical predictions, and laboratory experimental measurements of clouds with, $\rho_o/\rho_a = 4.19$, $D_o/H_o = 1.0$, and volumes as shown in liters, where $r1 = \rho_o/\rho_a$ and $r2 = D_o/H_o$.